Bivariate Moment Simulation of Coagulating and Sintering Nanoparticles in Flames

Daniel E. Rosner and Jouni J. Pyykönen
Dept. of Chemical Engineering, High Temperature Chemical Reaction Engineering Laboratory, Yale University, New Haven CT 06520

The design/control of particle synthesis reactors is hampered by the cumbersome nature of simulation methods (such as "sectional" representations of the particle population balance equation) to track the evolution of coagulating, restructuring populations in complex flow environments. Bivariate PBE-methods were investigated using generalizations of a recent Gaussian quadrature-based "moment" approach (McGraw, 1997; Wright et al., 2001). A 9-moment method was applied to an extensive data set recently obtained using a "seeded" laminar flame reactor with laser-based, as well as TEM-grid thermophoretic sampling. Alumina nano-aggregate population evolution is predicted using available rate/transport laws (for coagulation, thermophoresis and sintering) and the efficacy is predicted, and, together with the efficacy of such simulation methods for parameter estimation, is also illustrated inferring a "best fit" activation energy for nanoparticle sintering. Variants/extensions of these techniques should enable their incorporation into, say, full PDF-methods for turbulent synthesis reactors, using improved rate laws.

Introduction and Background

Particle morphology evolution; Bivariate aerosol populations

In many particle synthesis reactors of current interest, not only are particle *sizes* evolving in time or space, but so also is the particle morphology, due both to *coagulation* (to form aggregates) and to such *restructuring* rate processes as high temperature sintering. To describe or design such reactors it is therefore necessary to adopt a mathematical description that transcends the use of size alone as a particle "state variable," but, of course, one that remains computationally tractable. Moreover, even in laminar flow reactors, the local environment experienced by each particle in the population may change on a time scale not large compared to the mean time between successive coagulation events, thereby ruling out exploiting such occasionally useful approximations as "local self-preservation" for the "shape" of the required local particle distribution function [in one (Friedlander, 2000) or more (Tandon and Rosner, 1999) state variables]. In the present article, we initiate the theoretical study of the dynamics of such population evolution, using a recently developed class of "moment" methods (quadrature method of moments, QMOM) that can be extended to more complex flow fields. Our results are immediately compared here with an extensive set of experimental data based on our recently reported counterflow diffusion flame (CDF) studies of alumina nanoaggregate evolution (Xing et al., 1996, 1997, 1999). This study may also be regarded as an extension of our preliminary univariate modeling analysis in Xing et al. (1997).

BVQMOM simulation method and available data

For reasons that will become clear in the third section, we here adopt a "bivariate" (BV) description of particle state, extending the work of Koch and Friedlander (1990), who selected particle volume, v, and "wetted" surface area, a, as the state variables, using the difference, $a - a_{\min}(v)$, as the driving force for area reduction by particle sintering. The Gauss-

Correspondence concerning this article should be addressed to D. E. Rosner.

ian quadrature-based MOM we implement here (McGraw, 1997; Wright et al., 2001) has the following important attributes: It (A1) is free of any presumption about the *shape* of the particle number density distribution function, written $n(v, a; z)$, where z is an axial space variable in our CDF (Figure 1); (A2) allows the introduction of rate laws for coagulation and sintering of arbitrary complexity; and (A3) leads to evolution equations, governing a preselected subset of moments of $n(v, a; z)$, which are of the standard convective-diffusion form, and hence, generalizable to more complex flow fields using now-standard CFD techniques/software. Even though many of the local aerosol population descriptors measured/reported in Xing et al. (1996, 1997, 1999) are *not* proportional to simple moments of $n(v, a; z)$, our implementation of BVQMOM, using so-called RDGFA theory ("Results and Discussion"), allows us to predict these variations (such as the spatial distribution of 90 degree laser light scattering) for direct comparison with available data. This provides a valuable opportunity to initiate the systematic testing of alternate simulation methods based on the particle population-balance approach (Ramkrishna, 2000) in a nontrivial reactor flow environment, along with plausible, yet incompletely validated, rate laws for free-molecule regime coagulation, aggregate sintering, and axial thermophoretic transport (Gomez and Rosner, 1993; Filippov et al., 2000).

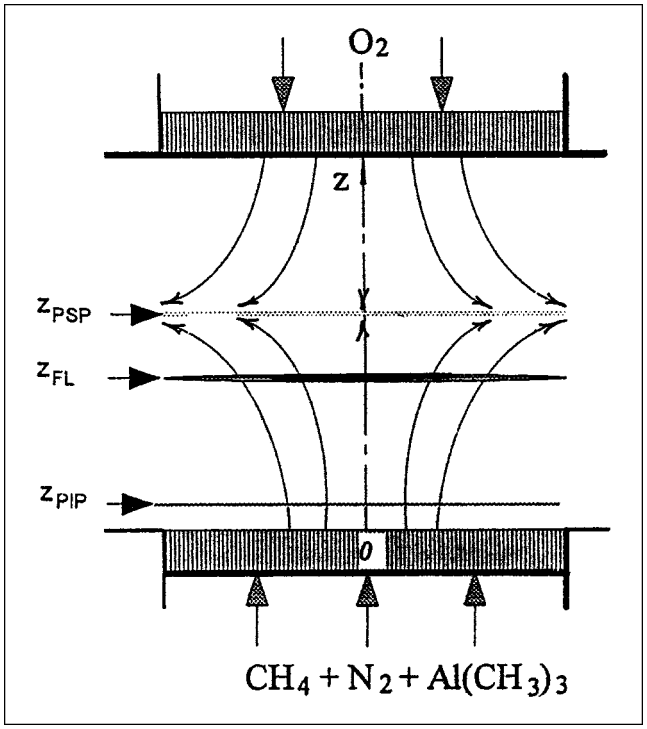

Figure 1. TMA-seeded laminar counterflow diffusion flame experimental configuration and notation.

After Xing (1997).

Objectives of present article: Foundation for rational sol reaction engineering

This "confrontation" of a comprehensive set of local CDF-structure measurements (using both laser-based *in situ* methods and thermophoresis-based "immersion" methods), with the predictions of a potentially versatile BVQMOM simulation technique, seems to us to be a long overdue necessary next-step in the development of sol reaction engineering (SRE) simulation methods capable of predicting/optimizing nanoparticle synthesis reactor performance, and guiding their future scale-up (Rosner, 2000). We make no claim that the present implementation of BVQMOM, with our present interim choice of rate laws ("'Observables' in Terms of v and a" and "Coagulation Rate Law") constitutes the last word in this line of attack. Rather, we will show that a plausible 3 quadrature point BV approach, equivalent to tracking nine moments of $n(v, a; z)$, combined with plausible but deliberately simplified rate laws (sections on coagulation rate law and sintering rate law), is able to capture most of the essential features of the observed sub-ppm volume fraction morphologically evolving alumina populations. As will be seen, in our TMA-seeded flames, low temperature (fuel-side) aggregation gives way to rapid sintering-coalescence near the ca. 2,300 K flame temperature, prior to exiting the flame structure near the particle stagnation plane (PSP; Gomez and Rosner, 1993) on the oxidizer side of the flame.

Experimental Database; Techniques

It will be useful to summarize here the nature of the seeded-flame experiments carried out in this laboratory, emphasizing the particle population characterization techniques exploited. However, this section will be deliberately concise, in view of our principal present objectives, and the availability of more complete descriptions of our equipment, methods, and two-phase flame structure results (Xing et al., 1996, 1997, 1999).

Burner system, choice of particle precursor; Flames studied

A slot laminar counterflow diffusion flame burner of the Katz type (Chung and Katz, 1985) has been constructed and used for the measurements utilized below (Xing et al., 1996, 1997, 1999). When continuously fueled with, say, gaseous methane containing small amounts of tri-methyl-aluminum (TMA) vapor and ignited in the presence of a counterflow of $O_2 + N_2$, one produces steady, locally flat, nonsooting diffusion flames, on the fuel side of which a population of alumina spherules in the ca. 12–30-nm-dia. range is formed as a result of rapid TMA hydrolysis. This population, here present at volume fractions less than ca. 0.3 ppm, immediately coagulates to form fractal-like aggregates (Figure 6 of Köylü et al., 1995; Figure 5 of Xing et al., 1997), which then sinter to form a distribution of larger spheres prior to their departure from the flame structure. These events occur within a vertical space of only ca. 8 mm, which has been probed with ca. 0.2-mm resolution using laser light scattering (the section titled "*In situ* Laser-Based ALS Measurements via RDGFA Theory) and ca. 0.5-mm resolution, using thermophoretic sampling/TEM image analysis techniques (TPS/TEM); (see the following section). The results of these measurements will

be displayed in "Results and Discussion," where direct comparisons with the predictions of our BVQMOM-simulation method are superimposed. TMA-seed levels were deliberately kept low enough so that the alumina particle population would exert a negligible influence of the "host" CH_4/air flame structure—that is, the coupling is "one-way," and the carrier gas temperature distribution, which exerts a strong effect on both aggregate sintering rates (Xing et al., 1996, 1997, 2000) and particle velocities due to axial "thermophoresis" (Eisner and Rosner, 1985; Gomez and Rosner, 1993; and as will be seen in Figure 3), could be probed using ca. 50-μm-dia. thermocouples in the absence of TMA-seeding. TMA was the particle precursor of choice because the resulting condensed alumina, considered $Al_2O_3(\alpha)$ with the corundum crystal structure, has well-studied macroscopic thermophysical/optical properties, and the decomposition of TMA leads to methyl radicals unlikely to dramatically alter the chemistry of these steady, atmospheric pressure, methane/air diffusion flames.

"Immersion" probing methods; TPS/TEM and TC-response

Rapid-insertion thermophoretic probing, followed by off-line TEM image analysis, was used to track Al_2O_3 nanospherule size evolution, as well as the aggregation and sintering rate processes. This technique exploits the size- and morphology-insensitivity of particle thermophoretic velocities in the free-molecule regime (Rosner et al., 1991; Zurita-Gotor et al., 2000) in the immediate vicinity of the initially cold probe carrying each 0.5 mm diam TEM grid. Our TPS-experimental procedures, patterned after those of Megaridis and Dobbins (1987) have been described in Köylü et al. (1995) and McEnally et al. (1998). Another thermophoretically based technique, that of thermocouple response to particulate deposition (Eisner and Rosner, 1985; McEnally et al. 1998), was also used to confirm the local alumina volume fraction (see Figure 4), free of any assumptions about alumina size- and morphology distributions, or optical properties. While these immersion methods lack the high spatial resolution of our laser light scattering measurements (see the following section), and are admittedly time-consuming, they provided essential complementary experimental information about these evolving, nonspherical, and nonabsorbing (@ 514.5 nm) alumina particle populations.

In situ laser-based ALS measurements via RDGFA theory

Angle-dependent laser light scattering measurements on an aggregating population of Rayleigh regime spherules provides valuable local information on aggregate size distributions, especially in the domain of "fractal-like" scattering behavior near, say, $D_f = 1.7$, as is expected for "cluster-cluster" Brownian aggregation in a wide variety of chemical systems (Dobbins and Santoro, 1988; Megaridis and Dobbins, 1990; Köylü and Faeth, 1993; Xing et al., 1999; Sorensen, 2001). These procedures, based on so-called Rayleigh-Debye-Gans fractal aggregate (RDG/FA) elastic light-scattering theory, were adopted here, using data obtained with a chopped CW argon-ion laser source operating at 514.5-nm wavelength. These measurements, which clearly revealed the locations of the "particle inception plane" (PIP) and "particle stagnation plane" (PSP), had an estimated spatial resolution of ca. 0.2 mm. Indeed, the high-quality LLS signal at a scattering angle of 90 degrees, provides a valuable test of any proposed theory of nonspherical particle evolution in such a flame reactor. This is especially true here because, on theoretical grounds, this signal is not simply proportional to any particular local "mixed"-moment of the distribution function $n(v, a; z)$—not even $M_{2\text{-}D_f,D_f}$ (which we show in "'Observables' in Terms of v and a" and "Results and Discussion," *would* be relevant in the so-called "power-law" regime, only if all aggregates in the population were sufficiently large, were characterized by the same fractal dimension, D_f, and had T-insensitive optical properties). Note that the local moment $M_{4,-3}$ would be relevant only if the spherules were *independent* Rayleigh scatterers.

Bivariate MOM Simulation Approach

v,a Description (Generalizations of Koch and Friedlander, 1990)

Considering the variety of partially sintered "aggregate" shapes that show up on our TEM images (Xing et al., 1995, 1996, 1997, 1999), it might seem that a description based only on the two particle state variables v and a has little chance of succeeding. However, in part because the area-equivalent diameter $(a/\pi)^{1/2}$, plays such an important role in transport theory (Rosner, 2000; Rosner et al., 2000), and systematic corrections due to nonsphericity (quantified here by the dimensionless sintering "driving force" $\xi \equiv [a/a_{\min}(v) - 1)]$ can also be introduced, it is remarkable how far one *can* go with only these two state variables (see below). Immediate questions arise about the relation of this choice of fundamental state variables to the now-familiar "fractal-like" characterization of particulate matter in coagulating systems with little or no sintering (Dobbins and Megaridis, 1987; Köylü et al., 1995; Brasil et al., 2000). For example, we do *not* choose the fractal "dimension" D_f as a fundamental state variable (cf. Kostoglu and Konstandopoulos, 1999), because we are using the results of RDGFA theory to interpret our experimental ALS signals. But, it is convenient for us to introduce an effective fractal dimension, $D_{f,\text{eff}}$, and corresponding "prefactor" $k_g(D_f)$, both defined (below) in terms of v and a. However, before introducing these, and our corresponding results for the effective aggregate gyration radius, and so forth, we note that a reasonable choice for mean *spherule diameter* d_1 within any aggregate is simply $6v/a = 6v_1/a_1$, independent of the (dimensionless) number, N, of such spherules, in the aggregate. This implies that we can define/calculate $N_{\text{eff}}(v,a)$ via v/v_1, so that

$$N_{\text{eff}} = a^3/\left[36(\pi)v^2\right] = \left[a/a_{\min}(v)\right]^3 \qquad (1)$$

(see, also, the section on nomenclature/list of symbols). Moreover, for a true fractal aggregate containing N equal-sized spherules, we find that its nonsphericity ξ is simply $[(N)^{1/3}] - 1$. Since, in our present work we rarely find aggregates containing more than about 125 spherules, this means that ξ will normally be much less than $5 - 1 = 4$. Indeed, for ξ values much above 1 the most likely morphology in our sampled flames *is* a fractal-like aggregate (Dobbins and

Megaridis, 1987; Köylü et al., 1995), with $D_f = 1.7$, containing more than eight spherules. This leads us, provisionally, to choose

$$D_{f,\mathrm{eff}}(v,a) = \begin{cases} 1.7 & \text{for} \quad \xi > 1 \qquad (2a) \\ 1.7 + (3-1.7)\cdot\cos(\pi\xi/2) & \text{for } \xi < 1 \qquad (2b) \end{cases}$$

ensuring that nearly spherical particles (with small ξ-values) will have effective D_f values near 3. By using our experimentally observed prefactor (ca. 2.3; Xing et al., 1997) for $D_f = 1.7$, and combining this value with the expected asymptotes for $D_f = 1$ ($(3)^{1/2}$) and, for the fully sintered $D_f = 3$, $N = 1$ limit, we suggest and use the following $k_g(D_f)$ interrelation

$$k_g(D_f) = (3)^{1/2} + 0.210(D_f - 1) + 2.29\left[(D_f - 1)/2\right]\cdot\left[(3 - D_f)/2\right] \qquad (3)$$

The preceding relationships lead immediately to the following expression for the effective gyration radius, $R_{\mathrm{gyr,eff}}(v,a)$

$$R_{\mathrm{gyr,eff}}(v,a) = (d_{1,\mathrm{eff}}/2)\cdot\left(N_{\mathrm{eff}}/k_g\right)^{1/D_{f,\mathrm{eff}}} \qquad (4)$$

which will be used in our prediction of laser light scattering (LLS) signals from our sintering populations of alumina particles. It remains for us to specify two additional important characteristic diameters for our nonspherical particles. One is the effective *collision* diameter for a particle with state variables v and a, which we provisionally take to be

$$d_{\mathrm{coll,eff}}(v,a) = \left[(D_f + 2)/D_f\right]^{1/2}\cdot(2R_{\mathrm{gyr,eff}}) \qquad (5)$$

It will be shown below ("Results and Discussion") that this choice, albeit plausible, seems to systematically underestimate our observed Brownian coagulation rates. The second is the projected area-equivalent aggregate diameter, $d_{a,\mathrm{proj,eff}}$, which is one of the quantities that has been measured directly from our TEM images. For the latter we take

$$d_{a,\mathrm{proj,eff}} = \left\{d_{i,\mathrm{eff}}\cdot N_{\mathrm{eff}}^{0.44}\right\}^{(3-D_f)/1.3}\cdot\left\{\left[a/(\pi)\right]^{1/2}\right\}^{(D_f-1.7)/1.3} \qquad (6)$$

which has the correct limiting behavior for both tenuous fractal aggregates (Cai and Sorensen, 1994) and dense spheres. Indeed, this effective diameter departs only slightly from $(a/\pi)^{1/2}$ for all shapes.

BVQMOM: Attributes and implementation; Numerical aspects

The simulation of an atmospheric pressure counterflow diffusion flame reactor producing "nanoparticles" involves the "free-molecule" Brownian coagulation kernel (which exhibits greater variations than in the continuum regime) as well as rapidly changing time scales for coagulation and sintering. Thus, the counterflow diffusion flame is a more demanding case for the bivariate QMOM than the idealized, constant time-scale continuum cases studied earlier (Wright et al., 2001). Indeed, we encountered computational diffculties with the versions of the bivariate quadrature scheme presented, and successfully exploited, in Wright et al. (2001). The causes of these difficulties were traced to the GAUCOF routine at the core of the quadrature scheme. To overcome these difficulties, we examined alternative ways to implement BVQMOM, giving special consideration to the requirements of simulating nanoparticle formation in our CDF environment. As a result, the following simplified 3-point variant of the quadrature scheme, equivalent to the use of nine moments, was developed.

To capture details of the evolution of the alumina nanoparticle population, the QMOM has been applied along the z-axis, here using the two particle state variables: volume, v, and *excess surface area*, $e \equiv a - a_{\min}(v)$. At each location along the z-axis, the "weights" (surrogates for the *pdf*(v,a) *ordinates*; Wright et al., 2001) are scaled according to local particle volume fraction ϕ_p, which is obtained from the predicted ω_p and ρ_g. QMOM-step sizes were determined adaptively, as described below. Mass fractions and environmental constants at the QMOM simulation points are obtained from CFD results (the section on uncoupled host flow field). These were smoothed with a polynomial fit to prevent spurious effects resulting from our "forcing" the temperature profile, $T(z)$, at a limited number of points near the peak temperature.

When devising the new implementation of the QMOM, we started by considering the demands on accuracy when predicting coagulation and restructuring in nanoparticle cases, which typically involve very high particle number concentrations. At high number concentrations, coagulation brings about a rapid growth in average particle size, which has a significant effect on restructuring rates. Therefore, inaccuracies in coagulation predictions are directly transmitted to particle shape evolution predictions. In contrast, the inverse effect (of the restructuring process on coagulation rates) is only of secondary importance. It is true that fractal-like particles have higher coagulation rates than spherical particles of equal volume, but coagulation rate predictions are not very sensitive to minor errors in restructuring predictions. Therefore, the starting premise for our present version of BVQMOM is that *coagulation* should be modeled as accurately as possible, and its accurate prediction is a prerequisite for simultaneous restructuring predictions. The univariate QMOM is rather accurate (McGraw, 1997). Therefore, we use a 3-point quadrature for pure volume moments as the principal quadrature. If we take the coagulation coefficients as given quantities, we get accurate predictions of coagulation this way.

A three-point quadrature for pure volume moments was used as a part of the original multiple three-point quadrature. The set of volume abscissas, v_i, and weights, w_i, obtained from the pure volume quadrature and moments $M_{1/3l}$, for $l = 1, 4/3, 5/3$, formed a linear system of equations, which was solved for the area abscissas, a_i. For the purposes of CDF analysis, we need to calculate a number of spatially varying intermediate quantities, such as the effective fractal dimension (which, in earlier studies, was assumed to remain constant throughout the simulation). With the 3-point quadrature, we have to rely on three representative points to provide data from which we can infer such quantities. Therefore, it is important that these points be as representative as possible. A problem with the earlier method was that there was no

guarantee that area abscissas were assigned values greater than that of a volume-equivalent sphere $a_{sph}(v)$. To enforce this necessary condition we switched from using area itself as the second state variable to area in excess of a volume-equivalent sphere, that is, $e \equiv a - a_{sph}(v)$. In the present implementation, the bivariate moments, $M_{k,l}$, are a set of mixed moments of volume and *excess* area, *defined* (for the purposes of this section only) as

$$M_{k,l} = \int_0^\infty \int_0^\infty \nu^k e^l n(\nu, e) d\nu \, de \tag{7}$$

An N-point quadrature expression for $M_{k,l}$ with quadrature points $\{\nu_i, e_i, w_i\}$ is

$$M_{k,l} = \sum_{i=1}^{N} \nu_i^k e_i^l w_i \tag{8}$$

Excess area abscissas, e_i, are determined from these moments in a similar manner to the way the area abscissas were determined in the original scheme. In our present implementation, we therefore have

$$M_{k,1/3} = \sum_{i=1}^{3} \nu_i^k e_i^{1/3} w_i \qquad k = 1, 4/3, 5/3 \tag{9}$$

This is a system of three linear equations in the three unknowns e_i, $i = 1, 2, 3$ that can be solved with v_i and w_i previously obtained from the pure volume moments.

The calculation of the evolution of the new mixed moments during coagulation is done in a fashion similar to actual areas, the difference being that the resulting new excess areas are now calculated as follows

$$e_{new} = e_1 + e_2 + a_{sph}(\nu_1) + a_{sph}(\nu_2) - a_{sph}(\nu_1 + \nu_2) \tag{10}$$

The N-point excess-area-based quadrature approximation for the bivariate moment evolution due to coagulation is now

$$\left[\frac{dM_{kl}}{dt}\right]_{coag} \approx \frac{1}{2} \sum_{i=1}^{N} \sum_{i=1}^{N} \Big\{ (\nu_i + \nu_j)^k \big[e_i + e_j + a_{sph}(\nu_j) - a_{sph}(\nu_i + \nu_j) \big]^l - \nu_i^k e_i^l - \nu_j^k e_j^l \Big\} \times \beta(\nu_i, \nu_j, e_i, e_j) w_i w_j. \tag{11}$$

A problem with any method that uses only a few moments is that other moments and derived quantities are not necessarily predicted with adequate accuracy. An aspect of special practical importance is that *conservation of area* during coagulation without restructuring (assumed in the model) is only approximate, and the method as written previously seems to have a tendency for small systematic errors for area that can distort our predictions. We, therefore, improved the accuracy of the method by numerically enforcing the conservation of area during coagulation. This was done by multiplying the excess area abscissas obtained from the mixed moments using Eq. 9 (denoted with a subscript *quad*) with a factor η, defined such that total area is forced to remain constant during coagulation

$$e_i = \eta e_{quad\ i} \tag{12}$$

where η is obtained using previous values of the abscissas denoted with a subscript *prev*

$$\eta = \frac{\overline{a_{prev}} - \overline{a_{sph}(\nu_{quad})}}{\overline{e_{quad}}} = \frac{\overline{e_{prev}} + \overline{a_{sph}(\nu_{prev})} - \overline{a_{sph}(\nu_{quad})}}{\overline{e_{quad}}} \tag{13}$$

Restructuring is modeled as a change in the excess area abscissas, with the rate-of-change determined by an equation (cf. Eq. 25) for excess area reduction due to sintering.

To deal with the problem of order-of-magnitude variations in the time-scales during coagulation, we have made the time/space step sizes in the program adaptive. Relative changes rates in the number of particles and the degree of sintering were used to determine the step sizes such that the *relative* changes remain small during each step.

We reiterate that in this study, our primary interest is in the coagulation and sintering behavior of the alumina nanoparticles, and we do not attempt to model (or measure) the details of their nucleation/vapor growth from the near-PIP reaction between TMA and water vapor (see, also, "Recommendations for Future Work"). Because the nucleated particles rapidly grow into the nondiffusive size range, we can neglect axial Brownian diffusion in this study (see the "Results and Discussion" section). Moreover, in the free molecular regime, particle thermophoresis can be assumed to be independent of particle size and morphology (Eq. 27 below). Thus, irrespective of their volume or area, all particles can be assumed to be transported axially at equal local velocity. These simplifications imply that, for modeling aggregate behavior in our laminar flame reactor, it is sufficient to consider the residence time-temperature history of this evolving particle *population*. A one-dimensional Lagrangian simulation along the z-axis from the particle inception plane to the particle stagnation plane can therefore be carried out for the assessment of aggregation/sintering models using our spatially resolved measurements ("Experimental Database"). On the downstream side of the particle inception plane, that is, at z_{PIP+}, the TMA-feed rate provides the initial alumina mass fraction via a balance on the chemical *element* Al (Rosner, 2000a). Since at this stage we do not model nucleation and other initial phases of particle formation, initial particle volumes and areas are given such that they agree with our data at the first measurement location at $z = 2$ mm, by which all particles are assumed to have already formed. The velocity profile (the section on the uncoupled host flow field) provides a natural boundary condition at z_{PSP}, the particle stagnation plane.

An additional consideration is the spreading of the flow around the z-axis when approaching the particle stagnation plane. This means that $\rho_g v_g$ is not constant along the z-axis and this must be accounted. One can think of a narrow con-

trol volume cell along the z-axis with constant dimensions in the y-direction. Part of the mass flow entering from below $\rho_g^- \nu_g^-$ does not leave the cell at the upper edge (+), but flows out through the sides of the cell. By subtraction, the mass flux through the sides of the cell is $\rho_g^- \nu_g^- - \rho_g^+ \nu_g^+$. This term needs to be accounted in all of the balance equations, including that for the particle mass fraction, ω_p. Since there are no significant temperature gradients in the y-direction (perpendicular to the z-axis), we have for the total particle mass balance

$$\omega_p^- \rho_g^- \nu_p^- = \omega_p^c \left(\rho_g^- \nu_g^- - \rho_g^+ \nu_g^+ \right) + \omega_p^+ \rho_p^+ \nu_p^+ \tag{14}$$

where ω_p^c is the particle mass fraction in the cell. Equation 14 can be solved numerically along the z-axis using the local environmental conditions provided by the CFD simulation. We have used an implicit scheme for estimating ω_p^c.

"Observables" in terms of ν and a; relevance of selected "mixed moments"

Consider any local "observable," $\mathcal{O}(z)$, which can be written in terms of a weighted integral over the joint number density distribution function $n(v, a; z)$

$$\mathcal{O}(z) = \int_0^\infty \int_0^\infty W(v, a) \cdot n(v, a; z) \cdot dv\, da \tag{15}$$

Clearly, whenever the relevant weighting function can be rigorously written or approximated, as a power-law in v and a with exponents k and l, respectively, then $\mathcal{O}(z)$ will simply be proportional to the local "mixed" moment $M_{kl}(z)$, where

$$M_{k,l}(z) \equiv \int_0^\infty \int_0^\infty v^k \cdot a^l \cdot n(v,a;z) \cdot dv\, da \tag{16}$$

As a consequence of their definitions, it is clear that the total local particle *number density*, $N_p(z)$ will be $M_{0,0}$, the total local *volume fraction*, ϕ, will be $M_{1,0}$, and the total area per unit volume, written a''', will be $M_{0,1}(z)$. Ratios of these particular moments therefore define the local population-mean particle volume ($\bar{v} = M_{1,0}/M_{0,0}$, and the corresponding *mean surface area* $\bar{a} = M_{0,1}/M_{0,0}$. We will also have occasion to use *dimensionless* mixed moments, $(\mu)_{kl}$, which plays the role of *jpdf* "shape factors" (Rosner et al., 2000). These are defined by

$$(\mu)_{kl} = M_{kl} / \left\{ [\bar{v}^k] \cdot [\bar{a}]^l \cdot [N_p] \right\} \tag{17}$$

Of course, because of the functional form $W(v,a)$, many observables *cannot* be concisely described in terms of one (or a small number of) particular mixed moment(s). This is especially true of the light scattering signal, say at 90 degrees, considered explicitly below, as well as other quantities, such as the rms R_{gyr}, inferred from our ALS data (Xing et al., 1999). An important attribute of the BVQMOM simulation method here is that, irrespective of the functional form of $W(v,a)$, any observable $\mathcal{O}(z)$ can be numerically obtained by a Gaussian quadrature, using the formal respresentation

$$\mathcal{O}(z) \cong \sum_i W(v_i, a_i) \cdot w(v_i, a_i) \tag{18}$$

where the indicated "weights" $w(v_i, a_i)$ are clearly related to the ordinates $n(v_i, a_i; z)$. When W *can* be written as a power law in v and a, then it is also clear that we will always be able to evaluate $\mathcal{O}(z)$ from the product of $W(\bar{v}, \bar{a})$, N_p, and the corresponding dimensionless moment μ_{kl} just defined. Thus, for example, we can always express

$$\bar{d}_1 = [6\, \bar{v}/\bar{a}] \cdot [(\mu)_{1,-1}] \tag{19}$$

$$\bar{N} = \left[\bar{a}^3 / \left(36(\pi) \bar{v}^2 \right) \right] \cdot (\mu)_{-2,+3} \tag{20}$$

where it must be kept in mind that the indicated *dimensionless* mixed moments are systematically different from unity (Rosner et al., 2000; Rosner and Yu, 2001; and Figure 9 below).

Returning to the BVQMOM prediction of the LLS signal, we note that the local scattered intensity, $I(z)$, at any scattering angle, θ, can be written in the form

$$I(z) = \text{const} \cdot \int_0^\infty \int_0^\infty N \cdot \left[(d_1)^6 \right] \cdot S \cdot n(v, a; z)\, dv \cdot da, \tag{21}$$

where the structure function $S(qR_1, N, D_f)$ is displayed in Figure 7 of Filippov et al. (2000), $q \equiv (4\pi/\lambda) \cdot \sin(\theta/2) = 0.017271\ \text{nm}^{-1}$ for $\theta = 90$ degrees, and we will introduce our "effective" values for $R_1 = d_1/2$, N_{eff} and $D_{f,\text{eff}}$, using a local Gaussian quadrature to evaluate the indicated double integral.

For our present purposes, we developed a simple but acceptable "curve-fit" for S, which can be written in the "pseudo-power-law" form

$$S = N^m \quad \text{if} \quad qR_1 < 1 \tag{22a}$$

$$S = 1 \quad \text{if} \quad qR_1 > 1 \tag{22b}$$

Here the (variable) exponent, m, is locally given by

$$m \approx 1 / \left\{ 1 + 0.0895 \cdot (\log_{10}(N)) / \left[(D_f) \cdot \log_{10}(1/(qR_1)) \right] \right\} \tag{23}$$

This has the correct behavior for both small qR_1(Guinier; where S approaches N), near-unity qR_1 (where $\log_{10} S$ approaches 1 with the log-log slope of $-D_f$), and the indicated const (0.0895) has been chosen to force graphical agreement at the "crossover point" shown in figure 7 of Filippov et al. (2,000) for the case $N = 120$. While *not* a simple power law in the state variables v and a, this relation [and the integral (Eq. 21)], have been used to generate the normalized $I(z)$ predictions (marked "full BVQMOM") in "Results and Discussion." It will also be instructive to compare the "full" $I(z)$ result with the limiting LLS cases of "Guinier" ($S = N$) and isolated spherules ($S = 1$). These latter presumptions lead to a normalized $I(z)$ proportional to the local mixed moments, $M_{4,-3}$ and $M_{2,0}$, respectively.

Finally, as a generalization of these limiting cases, it may be useful to note that, if the value of the "exponent" m just given is evaluated using only the local population averaged quantities: $\overline{N}$, $\overline{D}_f$, and $\overline{R}_1$ [as though $n(v, a; z)$ had no spread in either volume or area], then the predicted LLS signal, $I(z)$, would be locally proportional to the moment M_{kl} where $k = 6-2\cdot(\overline{m}+1)$ and $\ell = 3\cdot(\overline{m}+1)-6$.

Coagulation rate law

Because of their small size, especially compared with the gas molecule mean-free-path, l_g, near the thin flame (ca. 600 nm), we treat the aggregate-aggregate collision frequency using the bi-"molecular" kinetic theory rate $\beta_{fm,ij}$, with the effective collision diameters obtained from Eq. 5, assuming that every such encounter is "successful." Thus, for the BVQMOM simulations reported in "Results and Discussion," we use the second-order rate constant

$$\beta_{fm,ij} = \left(4/\sqrt{\pi}\right)\cdot\left[(8k_BT)/(\pi\rho_p)\right]^{1/2}\cdot\left[v_i^{-1}+v_j^{-1}\right]^{1/2} \cdot\left[(\pi/4)\cdot\left(d_{\text{coll},i}+d_{\text{coll},j}\right)^2\right] \quad (24)$$

The apparent need for future improvements of this choice will be discussed in "Results and Discussion" and the section on improved rate-laws, and Zurita-Gotor and Rosner (2001).

Sintering rate law

Following Koch and Friedlander (1990), we adopt a *sintering rate law* of the simple functional form

$$\dot{a} = -\left[a - a_{\min}(v)\right]/t_f \quad (25)$$

where, for the simulations reported below, we choose the local characteristic *fusion time*, t_f, to be of the surface diffusion-controlled form:

$$t_f = \left[k_BT\cdot(d_1/2)^4\right]/\left[24D_s\cdot v_m\cdot(\sigma)\cdot(\delta)\right] \quad (26)$$

seen to be proportional to the fourth power of $d_{1,\text{eff}} = (6v/a)$ and extremely sensitive to local temperature, mainly via the Boltzmann factor, $\exp(-E_{\text{diff}}/RT)$ governing the T-dependence of the diffusivity, D_s. In the nanospherule domain, we anticipate the need for systematic improvements of this expression for t_f (Xing and Rosner, 1999; Lehtinen and Zachariah, 2001). However, in keeping with our immediate objectives, these refinements (briefly discussed in the section on improved rate laws and transport property information) will be postponed to future extensions of this work. For the present, we content ourselves with illustrating ("Results and Discussion") how such BVQMOM simulations, when compared with our experimental data for, say, $\overline{N}(z)$, could ultimately be used to extract a best-fit value for the previously mentioned surface diffusion coefficient activation energy barrier, E_{diff}.

Neglect of axial Brownian diffusion

Outside of near-PIP and near-PSP "sublayers," as well as outside of the flame thickness itself (where V_T changes sign), which our present experimental methods cannot spatially resolve anyway, we can neglect the contribution that axial Brownian diffusion makes to the total axial velocity of the particles, $v_{p,z}(z)$. However, especially near the flame sheet, this velocity noticeably differs from the local gas velocity, $v_{g,z}(z)$, by the thermophoretic drift velocity, $V_T(z)$, which is fortunately insensitive to aggregate size and morphology (Rosner et al., 1991; Gomez and Rosner, 1993; Zurita-Gotor et al., 2000), being well-approximated by the Waldmann sphere result (for diffuse reflection and $Kn \gg 1$)

$$V_T(z) = 0.5385(\mu/\rho)_g\left[-\left(dT_g/dz\right)\right]/T_g\Big] \quad (27)$$

Here, $(\mu/\rho)_g$ is the local gas momentum diffusivity, estimated based on the local (measured) gas temperature, and the dominant local species compositions, as predicted from our FLUENT simulations of this CDF structure (see the following section).

We comment in "Results and Discussion" that, in the particle-laden domain between $z_{\text{PIP}+}$ and $z_{\text{PSP}-}$, axial Brownian diffusion contributes less than 0.02 percent of the total axial flux of particles. As an important corollary of this approximation, in the region experimentally probed, z becomes a "timelike" variable due to the absence of the term proportional to $D_p(v, a; z)\cdot d^2n/dz^2$ in the Eulerian population balance equation.

Uncoupled Host Flow Field: FLUENT-Calculated $v_{g,z}(z)$ and corresponding $v_{p,z}(z)$

To obtain the axial velocity profile of the gas along the z-axis, as well as a reliable estimate of the major species concentrations (such as to evaluate the local momentum diffusivity), a computational fluid dynamics (CFD) analysis of the CDF reactor was performed. Given our present purposes, this was a more attractive alternative to using tracer particle laser-velocimetry in the transverse direction, followed by a mass balance to reconstruct the corresponding axial *gas* velocity distribution (Gomez and Rosner, 1993). Now-standard methods of the CFD program FLUENT were used. In addition to normal laminar flow-convective diffusive equations for velocity components and enthalpy supplemented with the pressure correction equation, we solved convective-diffusive equations for the "major" gas phase species (N_2, O_2, CH_4, CO_2, CO, H_2O) mass fractions with source terms for combustion reactions. Methane combustion was simply modeled as a two-step mechanism, with CO as the intermediate species and Arrhenius parameters for methane decomposition taken from Jones and Lindstedt (1988) and, for CO decomposition, from Howard et al. (1970). The equations were solved in the two-dimensional $x = 0$ plane with a well-justified assumption of minimal side-"wall" effects near the center plane. As a starting point for the CDF simulation, we chose to rely on our TC-*measured* temperature data (Figure 2) and use these values as an *input* for the simulation. This was done by providing "penalty" source terms at a number of points along the z-axis that force the CFD solution toward the measured values. Also the gas stagnation plane was fixed in a similar manner such that the experimentally observed particle stagnation planes were obtained in the simulations. The limited degree of detail in our combustion chemistry model was deemed adequate since we rely on forcing agreement with the observed temperature profile, and the computed major species (see

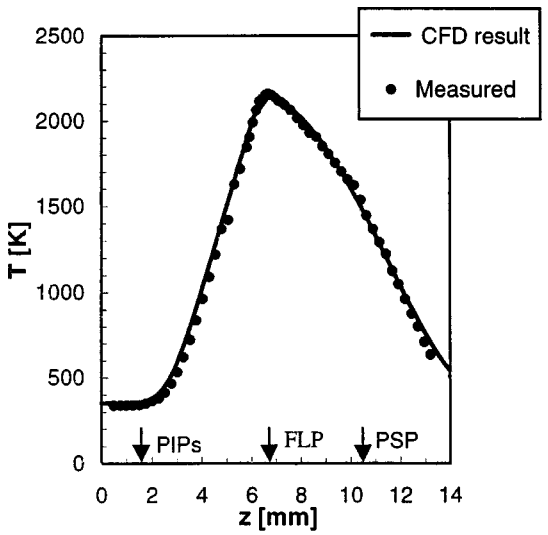

Figure 2. Thermocouple-measured gas temperature distribution, $T(z)$, within steady, laminar counterflow methane/"air" diffusion flame.

After Xing et al. (1996); Xing (1997).

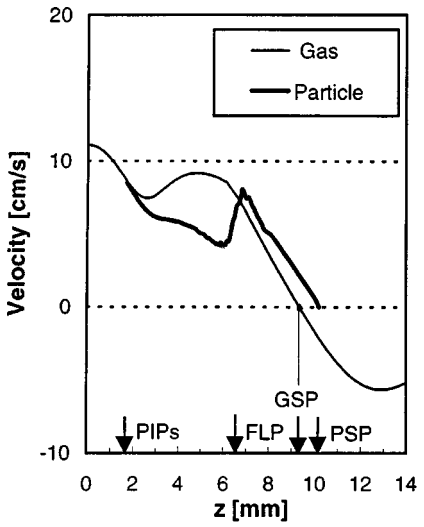

Figure 3. FLUENT-calculated host gas axial flow velocity field and predicted particle axial velocity distribution.

Allowing for axial particle *thermophoresis*.

earlier) will dominate the mixture viscosity and mass-density behavior.

Axial *particle* velocities will, of course, systematically deviate from the computed local *gas* velocity due to a thermophoretic drift in CDF regions where dT/dz is appreciable. For free-molecular regime particles, this thermophoretic velocity in the z-direction is adequately estimated using Eq. 27 (Gomez and Rosner, 1993; Zurita-Gotor et al., 2000). The time-temperature history of the alumina particle population, needed for our BVQMOM simulations (see the section on BVQMOM), is then obtained from this local particle velocity, v_p, which is the algebraic sum of the local FLUENT-computed gas velocity, v_g, and the local thermophoretic velocity drift along the z-axis (see Figure 3).

Results and Discussion

We turn now to predictions our formulation of BVQMOM dealing with measured aerosol population properties—both thermophoretically based and laser-based.

Figure 3 presents our calculated axial velocities for the host gas and the alumina nanoparticles. Since the thermal force pushes particles away from the hot flame, particle velocities on the fuel side are systematically smaller than gas velocities, but larger after passage through the flame. Axial temperature gradients are the largest on the fuel side, and this is where the thermophoretic "drift" velocity is the largest. It is noteworthy that thermophoretic velocity is also *relatively* large close to the particle stagnation plane. Incidentally, to assess the possible importance of buoyancy, we carried out some FLUENT simulations of CDF with disabled buoyancy. Based on these simulations, we conclude that buoyancy effects are only of secondary importance in the present case.

Our predictions for the spatial distribution of particle volume fraction ϕ (Figure 4) are in good agreement with the laser light scattering measurements. Initially, much of the decrease in volume fraction is due to thermal expansion of the host gas. However, across the flame "sheet" there is a dramatic drop in ϕ. This is a direct result of the thermal force that always pushes particles *away* from the FLP and, thus, increases particle concentration below z_{FLP} but decreases above z_{FLP}. The axial location of the concentration drop at the flame plane is, of course, predicted correctly, and so is the magnitude of the drop (here ca. half of a decade). In

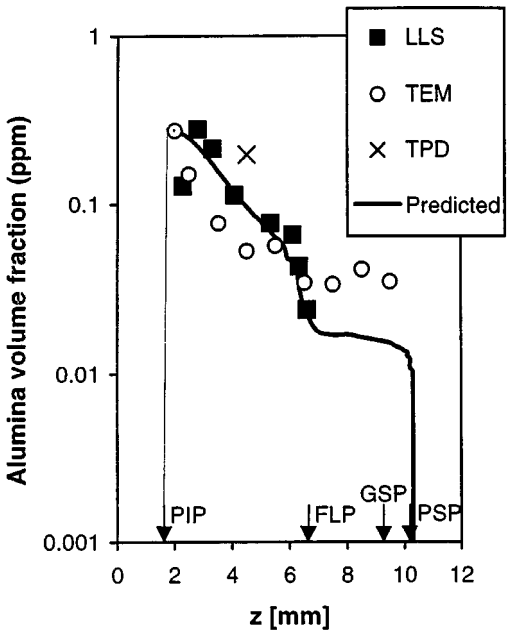

Figure 4. Measured (methods indicated) and BVQMOM-predicted alumina volume fraction ($M_{1,0}$) profiles.

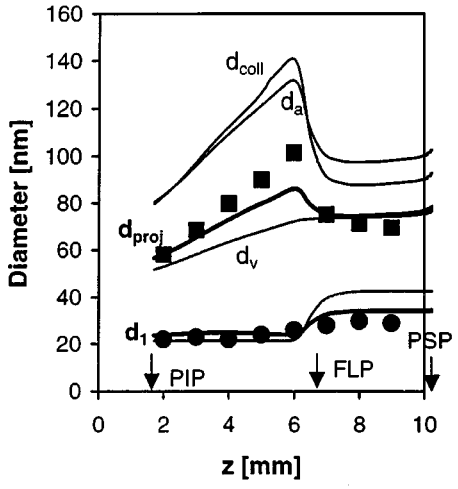

Figure 5. Measured and BVQMOM-predicted spherule- and aggregate-effective diameter evolution.

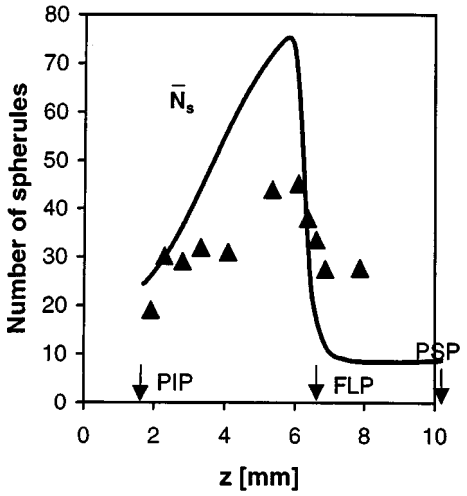

Figure 6. Measured and BVQMOM-predicted aggregate size [mean spherule number, $\bar{N}_s(z)$] evolution.

contrast, postflame TPS/TEM-based estimates of ϕ do not seem so accurate, probably because of the poorer spatial resolution of this "immersion" technique.

Figure 5 presents our BVQMOM predictions of the evolution of various population-averaged particle *diameters*. Predictions for mean projected area d_{proj} (aggregates) and mean *spherule* size d_1 are presented as bold lines. TPS/TEM-based experimental data for these quantities are also shown for comparison. The general accord of the d_1 (spherule) predictions with the measured values is a direct consequence of our best-fit selection for the activation energy for surface diffusion-controlled sintering (see Figure 7). One can note, though, that there is no clear increase in the measured *spherule* sizes at z_{FL} as a result of rapid local sintering, with the measured growth in spherule size being more gradual. The predictions for the *aggregate* dimension d_{proj} clearly do not indicate as much growth as the TEM images do. This seems to indicate that our present Brownian coagulation model (based on the collision diameter given by Eq. 5) underpredicts coagulation rates in our present implementation of BVQMOM. We also note that the values of d_a are very similar to the values of d_{coll}.

Figure 6 displays our predictions for the mean effective number of spherules per aggregate N_s. Note that N_s initially increases due to coagulation until near FLP when there is a marked decrease due to rapid sintering. Our predictions of this quantity seem to be rather sensitive to the initial (near-PIP) particle population. For example, small changes in the initial spread of this population resulted in large changes in the predicted level of the spherule number. Ironically, based on these particular results, it seems that the extent of coagulation has been overpredicted. The comparison with d_{proj} predictions is not straightforward, since the particle population is averaged in a different way in these predictions. However, qualitatively, the measured and predicted results for N_s are similar, with the location of rapid sintering predicted correctly.

Procedurally, the activation energy for sintering by surface diffusion can be obtained as a best-fit for simulation of the data from two flames with different TMA concentrations. Too small assumed activation energy values yield too large spherule sizes that sinter too early in the flame, while the resverse occurs with activation energy values that are too large. Figure 7 displays these differences in the predictions for the effective number of spherules, with three choices for this activation energy: 0.7 GJ/kg·mol, 0.8 GJ/kg·mol (optimum), and 0.9 GJ/kg-mol. Note that using 0.7 GJ/kg·mol, sintering takes place too early, and using 0.9 GJ/kg·mol, sintering does not bring about a major decrease in the number of particles. Looking at the final number of particles, a value slightly greater than 0.8 GJ/kg·mol would seem to be the optimum. However, for cases with the other flame, the optimum is slightly below 0.8 GJ/kg·mol. As a compromise, we have adopted the value 0.8 GJ/kg·mol, but further improvements must be introduced into our mathematical modeling of the sintering rate law (including a consideration of the "pre-exponential" terms, and morphological complexity) before this parameter can be assigned a molecular-level meaning.

Our BVQMOM predictions of the normalized LLS signal (at 90 degrees) are displayed in Figure 8, along with previously reported measurements (Xing et al., 1996, 1997, 1999). The curve marked "full BVQMOM" employs a compact curve-fit to the actual "structure factor" $[S(qR_1;\ D_f,\ N)]$ associated with fractal aggregates (according to RDG theory for assemblies of Rayleigh scattering spherules; see, e.g., Filippov et al., 2000, fig. 7). Since this function is by no means a power law in the particle state variables volume and area, and because the nature of our expressions for the effective values of R_1, D_f, and N (see the section titled "v, a Description"), the resulting $I(z)$ relation is proportional to no single mixed moment of $n(v, a; z)$. For comparison, instructive predictions are also shown for the extreme cases in which one "presumed" either isolated spherule scatterers ($S = 1$), or that all the elastic scattering took place far into the so-called "Guinier regime" (where $S = N$). In our present notation these two "idealized" $I(z)$ relations are therefore proportional to $M_{4,-3}$ and $M_{2,0}$, respectively. We see that the successful prediction of LLS intensity requires inclusion of the

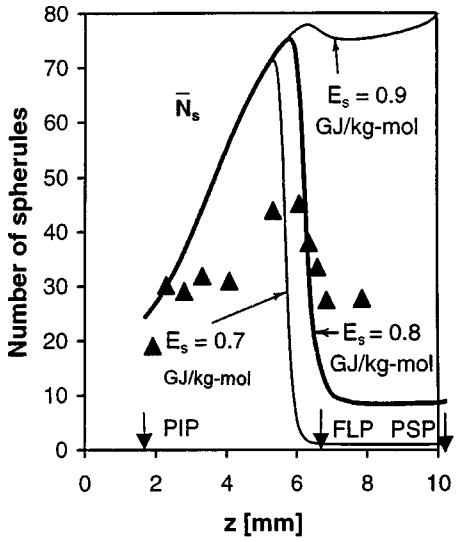

Figure 7. Inference of the sintering rate activation energy parameter, E_{diff}, via comparison of measured and BVQMOM-predicted alumina aggregate size [$\bar{N}_s(z)$] evolution.

aggregate structure factor. Even beyond the flame (between z_{FL} and z_{PSP}), predictions based on isolated Rayleigh spheres are particularly far from the mark.

Figures 9a, 9b have been constructed to display the fact that, as anticipated (Rosner and Yu, 2001), the parameter Dam_f is changing too rapidly in our flames to "permit" the assumption of "local self-preservation" with respect to volume and area. Rather than displaying the dimensionless distribution functions, $\bar{v}\bar{a}[n(v, a; z)]/N_p$ themselves, instead, we compare, in the spirit of moment methods, the dimensionless moment "surfaces," $(\mu)_{kl}$, on the k,l plane. Figure 9a shows

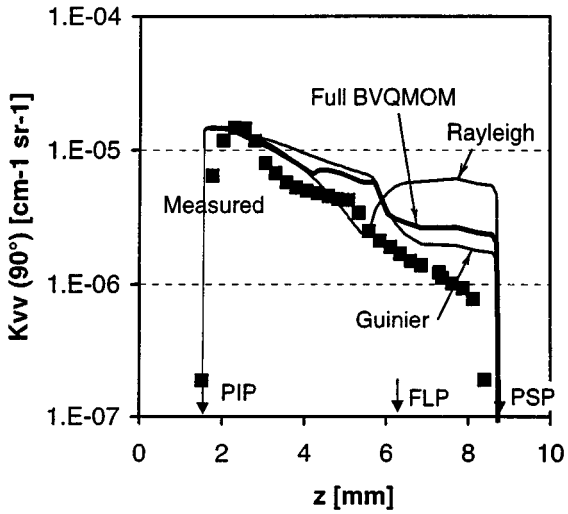

Figure 8. Measured and BVQMOM-predicted laser light scattering signals (normalized; scattering angle = 90 deg).

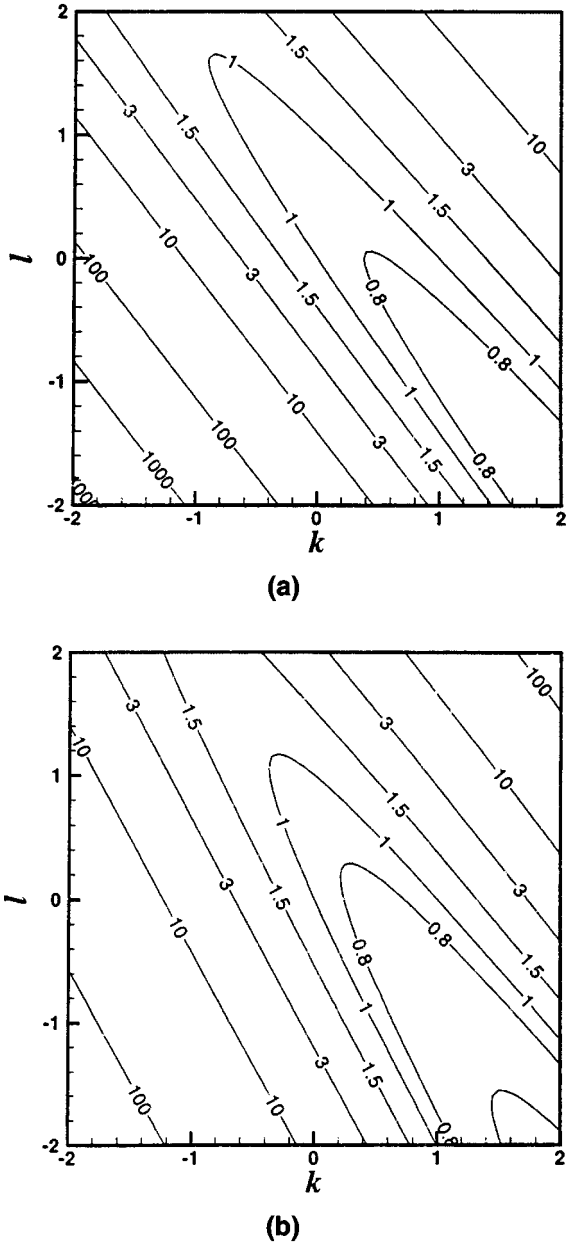

Figure 9. Local departures from "Bivariate Self-Preservation" via dimensionless mixed-moment "fingerprints" on the k,l plane.

(a) Assuming local "self-preservation" at $z = 4$ mm (flame #1; TMA feed rate: 0.8 mL/h); (b) BVQMOM-result at same location.

the appearance of this surface (via iso- μ_{kl} values, in the "self-preserving" limit, when Dam_f is large enough to incur significant sintering between collision events. In contrast, Figure 9b shows the same surface as computed using BVQMOM for the actual aggregate population achieved at $z = 4$ mm (Flame No. 1; TMA feed rate of 0.8 mL/h). Departures, especially in the direction of positive exponents k and l, are apparent, confirming our expectation that presuming a "local self-preservation" distribution function "shape" would *not* be

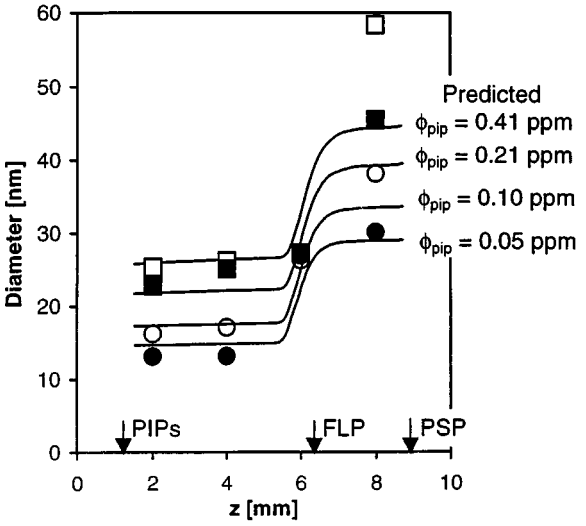

Figure 10. Measured- and BVQMOM-predicted dependence of mean spherule diameter on local particle volume fraction (via TMA seed level).

Open squares: measured at 0.41 ppm (at PIP); dark squares: measured at 0.21 ppm; open circles: measured at 0.1 ppm; dark circles: measured at 0.05 ppm.

a successful approach to modeling particle evolution in such "dynamical" environments, probably predicting poorly particle numbers in the large v and large a "tails."

Figure 10 displays our current predictions of the seed-level dependence of mean spherule size—a quantity measured rather directly from the TEM images obtained by thermophoretic sampling (section on immersion probing methods). Note that, provided one fixed $\bar{d}_1$ at the TPS-TEM measured values (at $z = 2$ mm), the BVQMOM predicts the remaining trends with position and volume fraction reasoanbly well. A challenging task for the future (and one that will require a full "near-PIP sublayer" analysis; see "Recommendations for Future Work" below) is to predict the seed-level dependence of $\bar{d}_1$ at the first measurement station.

Conclusions and Recommendations

Principal conclusions/implications

As a necessary next-step in the development of *Sol Reaction Engineering* simulation methods, not only capable of predicting/optimizing nanoparticle synthesis reactor performance, but also guiding their future scale-up (Rosner, 2000), we have "confronted" (in the preceding section) an extensive set of local 2-phase CDF-structure data (Xing et al., 1996, 1997, 1999; obtained using both laser-based *in situ* methods and thermophoresis-based "immersion" methods), with the predictions of a potentially versatile bivariate quadrature moment-based (BVQMOM) simulation technique. While, for simplicity, the present implementation of BVQMOM makes use of interim rate laws for coagulation and sintering ("'Observables' in Terms of v and a" and "Coagulation Rate Law"). The encouraging results shown/discussed in the previous section demonstrate that even a plausible 3-quadrature point BV approach, equivalent to tracking "only" nine moments of the joint pdf: $n(v, a; z)$, when combined with the deliberately simplified rate laws of the sections on coagulation rate and sintering rate laws, is able to capture most of the essential features of our observed morphologically evolving and coagulating alumina nanoparticle populations. Moreover, this has been demonstrated in a nontrivial laminar flow field with appreciable axial particle thermophoresis, in which particle heating and cooling rates are of the order of 30,000 K/s and in which low temperature aggregation (at sub-ppm volume fractions) gives way to rapid sintering-coalescence near the ca. 2,300 K flame temperature, prior to exiting the quasi-one-dimensional flame structure near the particle stagnation plane (PSP; Gomez and Rosner, 1993) on the oxidizer side of the diffusion flame. The results of this instructive test are especially encouraging because the Gaussian quadrature-based MOMs implemented here [the section on BVQMOM; and its immediate predecessors: McGraw, 1997; Wright et al., 2001] have the following attractive and probably indispensible features: They are (A1) free-of any presumption about the *shape* of the particle number density distribution function, written: $n(v, a; z)$; (A2) allow the introduction of rate laws for coagulation and sintering of arbitrary complexity; and (A3) lead to evolution equations, governing a preselected subset of moments of $n(v, a; z)$ of the standard *convective-diffusion* form, hence permitting generalization to more complex flow fields using now-standard CFD techniques/software. With further development we therefore believe that this class of new QMOM-based simulation methods will enable engineering predictions for even more complex nanoparticle synthesis reactors of industrial interest, including those that are multidimensional, turbulent, and even operating outside of the domain governed by the ideal (host-) gas law (see "Recommendations for Future Work" below).

Improved rate laws (coagulation and sintering) and transport property information

At least two aspects of the results reported here indicate that further systematic improvement of the input rate laws will be necessary. In "Results and Discussion" it was observed (cf. Figure 5) that the predicted rise in the population-averaged projected area-equivalent diameter of the alumina aggregates, especially between $z = 2$ mm ($T =$ 350 K) and $z = 6$ mm ($T = 2{,}000$ K), was noticeably less than the corresponding values based on image-analysis of the aggregate images appearing on our TEM grids. This suggests that Eq. 5, an approximation widely used to simulate fractal aggregate coagulation rates in uncharged aerosol systems at sub-ppm volume fractions, may systematically underestimate the effective collision diameter of these coagulating aggregates. While other possibilities may be considered, we are currently studying the encounters of computer-generated fractal aggregates to decide on a more accurate description of this important aggregate property (Zurita-Gotor et al., 2000). Of course, this systematic error will influence other morphologically sensitive predictions, including our prediction of the laser light scattering intensities (at, say, 90 degrees) shown in Figure 8.

Turning to the rate law for area reduction by high temperature sintering, we note that while Eqs. 25 and 26 evidently

can capture the aggregate "collapse" process, the "optimal" value of the energy barrier, E_{diff}, formally extracted from our simulations, equivalent to ca. 190 kcal/mol, seems rather large compared to values independently inferred for macroscopic alumina particle sintering under isothermal conditions, especially when the mechanism of *surface-diffusion* is dominant. Recently proposed refinements of the sintering rate law appropriate to *nano*aggregates (Xing and Rosner, 1999; Lehtinen and Zachariah, 2001), to be investigated in our follow-on research, are unlikely to be sufficient, since our spherule diameters were often as "large" as ca. 30 nm, containing of the order of a million Al_2O_3 "molecules." Rather, the required improvements may have to come from aggregate morphological considerations (departures from the 2-sphere limit), our investigation which was initiated in Rosner and Tandon (1997).

Turning finally to our particle transport property estimates, the level of agreement displayed (Figure 4) in our local volume fraction predictions, $\phi(z)$, suggests that our underlying assumption about the size and morphology insensitivity of the thermophoretic drift velocity are, indeed, sufficiently accurate. This has been confirmed by our independent MC-based aggregate-level predictions of orientation-averaged thermophoretic velocities (Zurita-Gotor et al., 2000), which are typically within 3 percent of the Waldmann single-sphere result, Eq. 27, exploited here. This remarkable conclusion, which of course underlies our use of "uncorrected" thermophoretic sampling probe data ("'Immersion' Probing Methods), is discussed in rather more detail in Rosner et al. (1991), and corroborated further in Gomez and Rosner (1993) and Zurita-Gotor et al. (2000).

Applications of BVQMOM to more complex flows?

Since the differential equations governing the selected bivariate moments, $M_{kl}(\mathbf{x}, t)$ are of the standard convective-diffusion form, our present BVQMOM formulation is readily extended to more complex flows, including those that are fully three-dimensional, and perhaps transient (to a fixed observer). We believe that the incorporation of these methods into more traditional CFD reactor modeling will be an attractive next step.

Recommendations for future work

It may be useful to conclude with a brief assessment of fruitful or instructive extensions of this work, based on our BVQMOM simulation and measurement experience to date. The recommendations below are certainly not exhaustive, nor are they presented in any order of "priority." They are merely comments on each of several important questions that we began to consider in the course of this work, but were, usually reluctantly, set aside. Indeed, we plan to address as many of them as possible in our subsequent work, also, of course, building on the experience of our colleagues in other laboratories.

"Effective Fractal Dimension" and a "Local Morphological Equilibrium" Conjecture. The unique relationship we have provisionally introduced between $D_{f,\text{eff}}$ and nonsphericity ξ (Eq. 2), while delightfully simple, we have to be relaxed in our future studies. The need is clearest when considering our optical and immersion probe experimental results early in the flame between ca. $z = 2$ mm and 4 mm, during which the aggregates appear to be growing in size (due to Brownian coagulation), and yet the optically inferred population-averaged $D_{\text{f,eff}}$ is also increasing, albeit slowly. An attractive possible generalization, which would remian computationally tractable, is to postulate a type of "local morphological equilibrium" (LME) condition, according to which the effective value of D_f, written $D_{\text{f,eff}}$ (v, a; environment), would respond to the local value of the Damkohler number for fusion, that is, t_{coag}/t_f for *that* particle. Here t_{coag} would be *its* mean time between encounters, and t_f would be *its* characteristic fusion time, and $D_{f,\text{eff}} = fct[Dam_f(v, a, \text{environment})]$ such that for $fct(0) = 1.7$, whereas $fct(\infty) = 3$. This type of LME postulate, which would also have possible applications in the modeling of crystallizers and related particle synthesis equipment, should be implemented and evaluated in follow-on studies. Of course, even LME will have its limitations, which remain to be delineated.

"Sublayer" Structure Analyses (Near-PIP,-FL and -PSP); Role/Evaluation of Axial Brownian Diffusivity. These three "sublayers," *not* well-resolved spatially by our present experimental techniques, each warrant more detailed theoretical attention. Indeed, in the language of "boundary layer theory" (see, e.g., Castillo and Rosner, 1996; Leal, 1992; Rosner, 2000), they are transition layers that must be matched to the observed "outer" profiles, which *have* been successfully probed (Xing et al., 1996, 1997, 1999), and treated theoretically in this article. The near-PIP sublayer, within which TMA hydrolysis, alumina particle nucleation, and vapor growth all occur, is of special interest here because we have measured the decisive spherule size distribution that "emerges" from it (near $z = 2$ mm). It is already clear that these spherules are too large, and too narrowly spread, to be the result of the conceptually simple Ulrich-Friedlander "coagulation" mechanism (according to which the chemically produced monomers are treated as nanoparticles that coagulate in the free-molecule regime until a mean size is reached at which fusion is unable to take place on the coagulation time scale (Xing and Rosner, 1999; Friedlander, 2000). In each of these sublayers differential axial Brownian diffusion may play a nonnegligible role. Indeed, this has motivated our recent MC-based studies on the relationship between orientation-averaged inverse mobility and the nonspherical particle state variables v and a (Rosner et al., 2000).

Further Seeded CDF-Experiments [Higher-TMA "Seed Levels" (Higher Particle Volume Fractions); TiO_2 Formation/Evolution in the Same Basic Flame Structure,...]. While, in these experiments and simulations, we have varied the alumina volume fraction by over about a 1-decade range up to ca. 0.6 ppm. It would be instructive to not only systematically study still higher TMA seed levels, but also to seed the same basic methane/air flames with precursors for other interesting inorganics, incluidng TiO_2, SiO_2, and, say, Fe_2O_3. Because of wide differences in volatilities, surface energies, and sintering rates, predicting the resulting variations in, say, observed spherule diameters would be a true test of our current understanding of the governing physicochemical processes and our present BVQMOM model, which is only applied here to Al_2O_3 data "alone." Even for our existing alumina experiments, we still have not made full use of the reported seed-level dependencies (Xing et al., 1996, 1997, 1999), which will

be part of our future work on the use of improved rate laws (see below).

Supplementary Laser-Based Particle Diagnostic Techniques; LII on Inorganics?. For studies in which nanoparticles of materials like Fe_2O_3 are synthesized in atmospheric pressure flames, it is also possible to supplement the laser light *scattering* techniques described in "*In situ* Laser-Based ALS Measurements via RDGFA Theory" by those exploiting the *absorption* of short (ca. < 10 ns), high-fluence (ca. 0.1 J/cm^2) laser light pulses (such as Nd-YAG at 532 nm). The resulting space- and time-resolved particle incandescence (LII) signals can be analyzed to yield local spherule size distributions (Filippov et al., 2000; Rosner et al., 2001) and, perhaps, local relative volume fractions. Indeed, this monitoring technique would open up the attractive prospect of nearly the real-time monitoring/control of spherule size—and, hence, particle-specific surface area, for such flame reactors. The results and implications of our recent LII experiments on iron-seeded laminar flames will be discussed in Rosner et al. (2001) and Schaffer (2001).

Measurements and Modeling of Additional Features of Combustion-Synthesized Nanoparticle Populations: Crystal Structure/Disorder, Spherule Surface Characterization, Interspherule Bond Strength. Depending on the application, there are particle attributes that may be of decisive industrial importance (say, for catalytic *surface* activity, rheology control, binding to a polymer "matrix," etc.) that have deliberately *not* been discussed thus far. Since most would require additional "state variables," and many have not been measured, even in our alumina experiments. Discussing their modeling would be premature. One such controllable attribute might be the distribution of interspherule bond energies in the flame-produced aggregates, symbolically described by $pdf(\epsilon_{11})$. But it remains to be determined whether this distribution (or at least the local mean value of ϵ_{11}) can be conveniently measured—perhaps using a combination of LLS and LII at fluences high enough to induce laser-induced aggregate breakup (LIABU)? This is one of several noteworthy possible extensions of LII, beyond the scope of this article, currently under investigation in our laboratories (Rosner, 2000; Rosner et al., 2001).

Consequences of Introducing Improved Rate Laws (Coagulation, Sintering). Suitably refined coagulation and sintering rate expressions (cf. Eqs. 5, 24, and 25, 26) should be able to noticeably improve the level of agreement already evident in Figures 4–8, describing our current round of BVQMOM simulations. Moreover, such comparisons can be used to test the accuracy of alternative proposals for the effective collision diameter of fractal-like aggregates (Zurita-Gotor and Rosner, 2000; Kazakov and Dryer, 2001), and also provide more realistic estimates of physicochemical parameters (such as E_{diff}, "Results and Discussion"), perhaps even those unobtainable by more conventional (e.g., isothermal furnace) measurements.

Initiating the Study of Trivariate Populations of Aerosol Particles; Is TVQMOM Feasible? Finally, as hinted earlier, there are many industrially important aerosol populations that will require a description that transcends the (present) use of "only" two state variables. While it is clear that MC-based simulation methods can readily deal with extensions to more than two state variables (Gooch and Hounslow, 1996; Rosner and Yu, 2001), it remains to be discovered whether BVQMOM can be conveniently extended to trivariate cases.

Summary

While the efficiency and accuracy of the BVQMOM was first demonstrated in a constant-environment, continuum regime case (Wright et al., 2001), the present CDF-study has demonstrated the need for further developments and "calibrations." In accord with the Gaussian quadrature philosophy underlying the efficiency of our methods, coagulation coefficients and observables are based only on their values at the calculated quadrature points. But, ironically, these approximations currently prevent us from drawing firmer conclusions on the validity of postulated physical laws governing, say, the aggregate coagulation and sintering rates. Thus, we view our evaluation of the activation energy for sintering ("Results and Discussion" and Figure 7) as only illustrative, because it is difficult to know how much of the disparity between predictions and experimental results for d_{proj} and $\bar{N}_s$ is related to the present BVQMOM simulation method, and how much to the embedded physical models. Clearly, detailed comparisons with accurate (albeit more time-consuming) sectional and/or MC predictions for cases like the ones studied here will be required in the near future.

Several "hybrid" techniques, which retain the attributes of each of their antecedents, should now be studied further. For example, Wright et al. (2001) has presented a technique, called MIDAS, for retrieving aerosol (optical) properties from the QMOM-calculated moments of the (univariate) spherical particle size distribution. In this technique, a set of smooth distributions (such as log-normals) *possessing the specified moments* is generated and then used to carry out needed integrals over the relevant number density distribution function. This clear departure from the Gaussian quadrature philosophy may be useful for certain future developments, since many nanoparticle properties *are* rather complicated functions of volume and (excess) area, and may not be adequately represented with weighting functions based only on estimation *at* a modest number of quadrature points. Indeed, some MIDAS-like technique might be used in the estimation of, say, coagulation rate coefficients to provide better coverage of the bivariate coagulation coefficient domain. While it is difficult to foresee these future developments in detail, we believe that new QMOM-based simulation methods of the type illustrated in this article will offer a practical route to more efficient design/optimization/scale-up methods for more complex particle synthesis reactors of industrial interest.

Acknowledgments

These bi-variate quadrature-based moment method (BVQMOM-) predictions of alumina nanoaggregate evolution in our seeded counterflow laminar flame experiments have been made possible by a Grant from NSF (Grant CTS 987 1885) as part of the Functional Nanostructures Program (M. C. Roco, Director). J. J. Pyykönen was a Visiting Graduate Assistant from VTT-Energy, Finland. His participation in the Yale HTCRE Lab research program during 2000 was made possible by a predoctoral grant from the Finnish Technology Development Center (TEKES). It is also a pleasure to acknowledge the helpful comments/correspondence of Drs. Robert McGraw, Douglas Wright, Juan Fernandez de la Mora, Jorma Jokiniemi, Chris

Sorensen, Mauricio Zurita-Gotor, Pushkar Tandon, and Yangchuan Xing.

Notation

a = particle surface *area*
$a_{\min}$ = minimum particle surface area *if particle were spherical with same volume*
a''' = aerosol population surface *area per unit volume* = $N_p \cdot \bar{a}$
$d_{a,\text{proj}}$ = projected area–equivalent aggregate diameter; Eq. 6
d_g = particle diameter corresponding to the volume v_g
d_l = spherule diameter ("primary" particles in aggregate)
d_{coll} = aggregate collision diameter; Eq. 5
D_p = Brownian diffusion coefficient for particle of volume v and area a
D_s = surface diffusion coefficient (units: m^2/s)
D_v = bulk diffusion coefficient (units: m^2/s)
D_f = fractal exponent ("dimension") describing morphology of aggregate population
E = activation energy barrier (aggregate restructuring; cf. section titled "*In situ* Laser-Based ALS Measurements via RDGFA Theory")
e = a-$a_{\min}(v)$; "excess" area variable; Eqs. 7–11
I = intensity of scattered laser light
k_B = Boltzmann constant
Kn_p = Knudsen number based on prevailing gas mean-free path and particle diameter
l_g = gaseous *molecule mean free path*
$M_{k,l}$ = k,lth moment of the *jpdf*: $n(v, a, \ldots)$; Eq. 16
m_p = mass of particle of volume v and area a
m = exponent appearing in N-dependence of structure factor; Eq. 22a
n = size distribution function $dN_p/dv \cdot da$
N_{eff} = number of "spherules" in an aggregate; $v/v_{1,\text{eff}}$; Eq. 1
N_p = total particle number density
$\mathcal{O}$ = observable; Eq. 15
q = $(4\pi/\lambda) \cdot \sin(\theta/2)$
R_1 = radius of spherule
R_{gyr} = gyration radius of aggregate
S = structure function for fractal aggregate; defined by Eq. 21
Sc = particle Schmidt number, $(\mu/\rho)_{\text{gas}}/D_p$
t_f = characteristic fusion (coalescence) time
T = absolute temperature (kelvins)
u = particle volume (dummy variable); see, also, v'
v = vertical velocity of mixture (z-direction)
v = volume of condensed material in spherical particle or aggregate
V = drift velocity
v_g = geometric-mean particle volume in log-normal PSD $n(v, \ldots)$
$\bar{v}$ = mean particle volume, ϕ_p/N_p, of local aerosol
$v_{1,\text{eff}}$ = effective spherule volume, computed from $d_{1,\text{eff}} = 6v/a$
v_m = average molecular volume in condensed state
$W(v,a)$ = weighting factor; Eq. 15
w_i = "weights" representing (prop. to) the PSD "ordinates"

Greek letters

$\beta(u,v)$ = coagulation rate constant in "mass-action" law (used to calc. coag. time)
δ = effective thickness of surface layer; approx.: $3(6v_m/\pi)^{1/3}$
η_1 = dimensionless particle *volume*, $v/\bar{v}(t)$
η_2 = dimensionless particle *area*, $a/\bar{a}(t)$
ϕ_p = particle volume fraction; $\bar{v} \cdot N_p$
ω_p = local particle mass fraction
ξ = nonsphericity parameter
λ = wavelength of laser light
θ = light scattering angle
ρ_p = intrinsic density of a particle (m_p/v_p)
μ_{kl} = dimensional "mixed" moment of dimensionless PSD: ψ_{12}
μ_{gas} = dynamic Newtonian viscosity of the carrier gas
μ = dynamic Newtonian viscosity of condensed material
ψ_1 = dimensionless unconditional *pdf* with respect to rescaled *volume*, v
ψ_2 = dimensionless unconditional *pdf* with respect to rescaled dimensionless *area*, a
ψ_{12} = dimensionless joint *pdf* with respect to dimensionless volume and area; $\bar{v} \cdot \bar{a} \cdot n(v,a)/N_p$
σ_g = geometric standard deviation of unconditional pdf with respect to v or a
σ = surface energy ("tension") of condensed material
ν = momentum diffusivity ("kinematic viscosity") of the carrier gas, $(\mu/\rho)_{\text{gas}}$

Subscripts and superscripts

BU = break up
c = continuum limit ($Kn_p \ll 1$) (see, e.g., Tandon and Rosner, 1999)
c = pertaining to the cell (Eq. 14)
coag = coagulation
coalesc = coalescence
eff = effective value
f = fusion (coalescence), or "fractal"
fm = free-molecule limit ($Kn_p \gg 1$)
g = pertaining to log-normal PSD (geometric)
gas = pertaining to the carrier gas
gyr = gyration
k,l = pertaining to moment exponents k,l, where k,l need *not* be an integer, nor positive
m = pertaining to a single molecule
max = maximum value
p = particle(s)
ref = reference value
T = thermophoretic
1 = pertaining to the "primary" spherules (e.g., $d_{1,\text{eff}} = 6v/a$)
1 = pertaining to particle *volume* (cf. area), as in η_1, ψ_1
2 = pertaining to particle *area* (cf. volume) as in η_2, ψ_2
+,− = evaluated on the + or − side

Other

$(\,)''$ = per unit area
$(\,)'''$ = per unit volume
$\dot{(\,)}$ = time rate of change
$\overline{(\,)}$ = mean value of $(\,)$ (e.g., $\bar{v}$, $\bar{a}$, $\overline{N}$, …)
$(\,)'$ = dummy variable, as in $\beta(v,v',a,a')$ pertaining to collision partner
$\min(a, b)$ = the lesser of a, b
$|$ = conditioned on (given:)

Abbreviations/acronyms

ALS = angle-dependent (laser) light scattering
BV = bivariate (2-state variables)
c = continuum limit ($Kn_p \ll 1$)
coag = pertaining to (Brownian) coagulation
CFD = computational fluid dynamics
CDF = counterflow diffusion flame (see, e.g., Xing et al., 1996, 1997, 1999)
CPU = central processor unit
Dam = Damkohler number (characteristic *time* ratio): Here $t_{\text{coag}}/t_{\text{fusion}}$
FA = fractal-like aggregate
fm = free-molecule limit ($Kn_p \gg 1$)
Fct. = function
FL = evaluated at the flame position; Figures 1 and 2
GAUCOF = Gaussian coefficient subroutine
IPDE = integro partial density function
jpdf = joint probability density function (here bivariate)
LII = laser-induced incandescence
LIABU = laser-induced aggregate breakup
LLS = laser light scattering
LME = local morphological equilibrium; section titled "Recommendations for Future Work"
MC = Monte Carlo (simulation method)
MOM = method of moments
Nd-YAG = neodymium-yttria-stabilized garnet laser

mfp = gaseous *molecule mean free path*
ODE = ordinary differential equation
PIP = particle inception plane; Figures 1 and 2
pdf = probability density function (normalized)
PSD = particle size (volume) distribution
PSP = particle stagnation plane position; Figure 4
QMOM = quadrature method of moments
RDGFA = Rayleigh–Debye–Gans–fractal aggregate (theory)
RHS = righthand side
rms = root mean square
SRE = sol reaction engineering
TC = thermocouple
TEM = transmission electron microscopy
TMA = trimethyl aluminum (vapor precursor)
TPD = thermocouple particle "densitometry"
TPS = thermophoretic sampling
TV = trivariate

Literature Cited

Brasil, A., T. Farias, and M. Carvalho, "A Recipe for Image Characterization of Fractal-like Aggregates," *J. Aerosol Sci.*, **30**, 1379 (1999).

Cai, J., and C. M. Sorensen, *Phys. Rev. E*, **50**, 3397 (1994).

Castillo, J. L., and D. E. Rosner, "Role of High Activation Energy Homogeneous Chemical Reactions in Affecting CVD-Rates and Deposit Quality for Heated Surfaces," *Chem. Eng. Sci.*, **51**, 5325 (1996).

Chung, S. L., and J. K. Katz, "The Counterflow Diffusion-Flame Burner: A New Tool for the Study of the Nucleation of Refractory Compounds," *Combust. Flame*, **61**(3), 271 (1985).

Diemer, R. B., and J. H. Olson, "A Moment Methodology for Coagulation and Breakage Problems: I. Analytical Solution of the Steady State Population Balance," *Chem. Eng. Sci.* (2001a).

Diemer, R. B., and J. H. Olson, "A Moment Methodology for Coagulation and Breakage Problems: II. Moment Models and Distribution Reconstruction," *Chem. Eng. Sci.* (2001b).

Dobbins, R. A., and C. M. Megaridis, "Morphology of Flame-Generated Soot as Determined by Thermophoretic Sampling," *Langmuir (ACS)*, **3**, 254 (1987).

Dobbins, R. A., R. J. Santoro, and H. J. Semerjian, "Analysis of Light Scattering from Soot Using Optical Cross-Section for Aggregates," *Proc. Int. Comb. Symp.*, The Comb. Inst., Pittsburgh, PA, p. 1524 (1990).

Eisner, A. D., and D. E. Rosner, "Experimental Studies of Soot Particle Thermophoresis in Non-Isothermal Combustion Gases Using Thermocouple Response Techniques," *Combust. Flame*, **61**, 153 (1985).

Filippov, A. V., M. W. Markus, and P. Roth, "*In Situ* Characterization of Ultra-Fine Particles by Laser-Induced Incandescence Sizing and Particle Structure Determination," *J. Aerosol Sci.*, **30**, 71 (1999).

Filippov, A. V., M. Zurita, and D. E. Rosner, "Fractal-Like Aggregates: Relation Between Morphology and Physical Properties," *J. Colloid Interface Sci.*, **229**, 261 (2000).

Friedlander, S. K., *Smoke, Dust and Haze*, 2nd ed., Oxford Univ. Press, Oxford (2000).

Gomez, A., and D. E. Rosner, "Thermophoretic Effects on Particles in Counterflow Laminar Diffusion Flames," *Comb. Sci. Tech.*, **89**, 335 (1993).

Gooch, J. R., and M. D. Hounslow, "Monte-Carlo Simulations of Size Enlargement Mechanisms in Crystallization," *AIChE J.*, **47**, 1864 (1996).

Howard, J., G. Williams, and D. Fine, "Kinetics of Carbon Monoxide Oxidation in Post-Flame Gases," *Proc. Symp. (Int.) on Combustion*, The Combustion Institute, Pittsburgh, PA, p. 975 (1972).

Jones, W., and R. Lindstedt, "Global Reaction Schemes for Hydrocarbon Combustion," *Combust. Flame*, **73**, 233 (1988).

Kazakov, A., and F. Dryer, "Aerosol Aggregation Kinetics and Its Implications for the Interpretation of Soot Optical Measurements," Second Joint Meeting of the U.S. Sections of the Combustion Institute, Oakland, CA (2001).

Koch, W., and S. K. Friedlander, "The Effect of Particle Surface Coalescence on the Surface Area of a Coagulating Aerosol," *J. Colloid. Interface Sci.*, **140**, 419 (1990).

Kostoglu, M., and A. G. Konstandopoulos, "Brownian Coagulation of Fractal Aggregates," *J. Aerosol Sci.*, **31**, (Suppl. 1), S574 (2000).

Köylü, Ü., Y. Xing, and D. E. Rosner, "Fractal Morphology Analysis of Combustion-Generated Aggregates Using Angular Light Scattering and Electron Microscopy Images," *LANGMUIR*, **11**, 4848 (1995); also, Köylü, Ü. O., and G. M. Faeth, *Combust. Flame*, **89**, 140 (1992).

Köylü, Ü., O., C. S. McEnally, D. E. Rosner, and L. D. Pfefferle, "Simultaneous Measurements of Soot Volume Fraction and Particle Size/Microstructure in Flame Using a Thermophoretic Sampling Technique," *Combust. Flame*, **110**, 494 (1997).

Leal, L. G., *Laminar Flow and Convective Transport Processes*, Butterworths-Heinemann, Stoneham, MA (1992).

Lehtinen, K. E. J., and M. R. Zachariah, "Effect of Coalescence Energy Release on the Temporal Shape Evolution of Nano-particles," *Phys. Rev. B*, **63**, 205402 (2001).

McEnally, C., Ü. O. Köylü, L. D. Pfefferle, and D. E. Rosner, "Soot Volume Fraction and Temperature Measurements in Laminar Non-Pre-mixed Flames Using Thermocouples," *Combust. Flame*, **109**, 701 (1997).

McGraw, R., "Description of Aerosol Dynamics by the Quadrature Method of Moments (QMOM)," *Aerosol Sci. Technol.*, **27**, 155 (1997).

Megaridis, C., and R. A. Dobbins, "Morphological Description of Flame-Generated Materials," *Combust. Sci. Tech.*, **71**, 95 (1990).

Ramkrishna, D., *Population Balances—Theory and Applications to Particulate Systems in Engineering*, Academic Press, Orlando, FL (2000).

Rogak, S., H. Nguyen, and R. Flagan, "The Mobility and Structure of Aerosol Agglomerates," *Aerosol Sci. Technol.*, **18**, 25 (1993).

Rosner, D. E., D. W. Mackowski, and P. Garcia-Ybarra, "Size-Insensitivity and Estructure-Insensitivity of the Thermophoretic Transport of Aggregated Soot Particles in Gases," *Combustion Sci. and Technol.*, **80**, 87 (1991).

Rosner, D. E., and P. Tandon, "Sintering Kinetics and Transport Property Evolution of Large Multi-Particle Aggregates," *Chem. Eng. Commun.*, **151**, 147 (1996).

Rosner, D. E., P. Tandon, R. L. McGraw, and D. Wright, "Relevant 'Mixed'-Moments for the Calculation of Deposition, Vapor Scavenging, and Optical Properties for Populations of Non-spherical Suspended Particles," *Proc. 4th Int. Particle Technology Forum*, (Nov. 2000) (available in CD, Session T1d08).

Rosner, D. E., and S. Yu, "Monte-Carlo Simulation of Free-Molecule Regime Brownian Aggregation and Simultaneous Spheroidization," *AIChE J.*, **47**, 545 (2001).

Rosner, D. E., *Transport Processes in Chemically Reacting Flow Systems*, Dover, Mineola, NY (2000a).

Rosner, D. E., "Aerosol Reaction Engineering: Measuring and Modeling the Performance of Combustion-Synthesized Nano-Particle Reactors," AAAR 2000, St. Louis, MO (2000b).

Rosner, D. E., A. Schaffer, M. B. Long, and B. La Mantia, "*In-Situ* Real-Time Sizing of Inorganic Nano-Particle Populations in Flames Using Laser-Induced Incandescence," *AAAR2001*, Portland, OR (2001).

Roth, P., and A. V. Filippov, "*In Situ* Ultra-Fine Particle Sizing by a Combination of Pulsed Laser Heat-Up and Particle Thermal Emission," *J. Aerosol Sci.*, **27**, 95 (1994).

Schaffer, A., *Quantitative Characterization of Species, Temperature and Particles in Steady- and Time-Varying Flames by Optical Methods*, PhD Diss., Yale University, New Haven, CT (2001).

Sorensen, C. M., "Scattering Light by Fractal Aggregates: A Review," *Aerosol Sci. Tech. AAAR*, **35**(2), 640 (2001).

Tandon, P., and D. Rosner, "Monte-Carlo Simulation of Particle Aggregation and Simultaneous Restructuring," *J. Colloid Interface Sci.*, **213**, 273 (1999).

Wang, G. M., and C. M. Sorensen, "Diffusive Mobility of Fractal Aggregates Over the Entire Knudsen Number Range," *Phys. Rev. E*, **60**, 3036 (1999).

Wright, D., R. McGraw, and D. E. Rosner, "Bivariate Extension of the Quadrature Method of Moments for Modeling Simultaneous Coagulation and Sintering of Particle Populations," *J. Colloid Interface Sci.*, **236**, 242 (2001).

Xing, Y., *Synthesis and Morphological Evolution of Inorganic Nanoparticles in Gas Phase Flames*, PhD Diss., Chemical Engineering Dept., Yale University, New Haven, CT (1997).

Xing, Y., Ü. Köylü and D. Rosner, "Synthesis and Restructing of Inorganic Nanoparticles in Counterflow Diffusion Flames," *Combust. & Flame*, **107**, 85 (1996).
Xing, Y., Ü. O. Köylü, and D. E. Rosner, "*In situ* Light-Scattering Measurements of Morphologically Evolving Flame-Synthesized Oxide Nano-Aggregates," *Appl. Opt.*, **38**, 2686 (1999).
Xing, Y., and D. E. Rosner, "Prediction of Spherule Size in Gas Phase Nanoparticle Synthesis," *J. Nanoparticle Res.*, **1**, 1 (1999).
Xing, Y., D. E. Rosner, Ü. O. Köylü, and P. Tandon, "Morphological Evolution of Nanoparticles in Diffusion Flames: Measurements and Modeling," *AIChE J.*, **43**, 2641 (1997).
Xiong, Y., and S. E. Pratsinis, "Formation of Agglomerate Particles by Coagulation and Sintering: I. A Two-dimensional Solution of the Population Balance Equation," *J. Aerosol Sci.*, **24**, 282 (1993).
Zurita-Gotor, M., A. V. Filippov, and D. E. Rosner, "Quasi-Monte-Carlo Calculations of the Transport Properties of Fractal-Like Aggregates in the Free-Molecular Regime," *Proc. AAAR2000*, Portland, OR (2000).
Zurita-Gotor, M., and D. E. Rosner, "Calculations of the Effective Diameter for Collisions of Fractal-like Aggregates," *Proc. AAAR2001*, St. Louis, MO (2000).
Zurita-Gotor, M., and D. E. Rosner, "Effective Diameters for Collisions of Fractal-Like Aggregates: Recommendations for Improved Aerosol Coagulation Frequency Calculations," *Proc. Nat. Aerosol Symp.*, Helsinki, Finland, 146 (2001).

Manuscript received Mar. 13, 2001, and revision received Sept. 14, 2001.